

## **6. FLUID DYNAMICS IN HIGH PRESSURE SLURRY BUBBLE COLUMNS**

### **6.1. Introduction**

In this work at OSU a study of hydrodynamic characteristics of high-pressure and high-temperature bubble columns were undertaken. The PIV technique was utilized to quantify the rise velocity and interactive dynamics of bubbles. In this report, the flow visualization technique using the PIV's unique particle tracking algorithm and blob size analysis is used to investigate the single bubble rise velocity and the bubble size distribution in a high-pressure bubble column. Furthermore, a computational model for gas-liquid-solid fluidization systems and a two-dimensional code based on it are developed in this study. In this model, the volume-averaged method, the dispersed particle method and the volume-of-fluid method are used, respectively, to account for the flow of liquid, solid, and gas phases. The gas-liquid interfacial mass, momentum, and energy transfer is described by a continuum surface force model. A collision model, which includes the particle-fluid and particle-particle interactions during the entire process of collision, is considered in the simulation. The particle-bubble interaction is formulated by incorporating the surface tension force in the equation of motion of the particles. The simulation of a single bubble rising in a liquid-solid fluidized bed and the particle entrainment with an emerging bubble is conducted and the results are in good agreement with the experimental findings.

### **6.2. Experimental Set-up**

The high-pressure and high-temperature bubble column system used in this study consists of a vertical column, a liquid supply tank, a liquid exhaust reservoir, a piston pump, and a pulsation damper. The vertical column comprises three sections: the plenum, the test, and the disengagement sections. The pipes and column are insulated. Two sizes of stainless steel columns are used: one is 50.8 mm in diameter and 0.80 m in height and the other is 101.6 mm in diameter and 1.58 m in height. The latter is specifically used for the bubble rise velocity measurement. In both columns, there are three pairs of planar quartz windows with dimensions of 12.7 mm in width and 92 mm in height. These windows allow viewing through the entire test section of the column. The plane shape circumvents optical distortion in photography.

Nitrogen is used as the gas phase and as the pressurizing source. The inlet pressure is regulated by a two-stage regulator, and the flow rate is controlled by a flow control valve. To maintain a constant system temperature, nitrogen is preheated by a gas heater to the desired temperature before being introduced into the column. Nitrogen enters the bubble column through a multi-orifice sparger in a ring arrangement with an orifice diameter of 3 mm. After exiting the bubble column, the gas passes through a back pressure regulator, which is used to control the pressure of the column. It is then ventilated into the atmosphere through the demister and the cooling tank. The gas flow rate is measured with either an electromagnetic gas flow meter or a rotameter at the end of the gas exhaust line. Paratherm NF heat transfer fluid, a stable organic liquid ( $T_b = 327^\circ\text{C}$  at 0.1 MPa), is used as the liquid phase. The liquid is operated in a batch mode. The liquid level in the column is maintained near the top of the column so that foaming will not affect the global-scale measurements.

A high-speed PIV system developed in-house is used to analyze the characteristics of bubbles. The CCD image picked up on the high-speed camera features 765 pixels across by 246 lines. The framing rate of the camera can be selected up to 480 fields/sec. A frame grabber, which is equipped with 40 MHz maximum pixel clock to support the high-framing rate, simultaneously digitizes the CCD image from the camera. Further, the high-speed camera is connected to the high-speed video recorder to store the images for further studies. The PIV technique used here relies on a particle-tracking algorithm (Chen and Fan, 1992) to determine the velocity fields of the particles. The particle-tracking algorithm involves matching the same objects in three or more consecutive fields.

### 6.3. Single Bubble Rise Velocity

The rise velocity,  $U_b$ , of single bubbles of known sizes is measured at various pressures ranging from 0.1 to 19.4 MPa for three temperatures, 27, 47 and 78°C. The bubble size is represented by the equivalent spherical diameter,  $d_e$ . The results are shown in Figure 6.1 for 27°C and 78°C. As shown in the figure, for a given bubble size,  $U_b$  tends to decrease with increasing pressure at both temperatures. To elucidate the effects of pressure and temperature, or more directly, the effects of physical properties of the gas and liquid phases on the variation of  $U_b$  with  $d_e$ , the following three predictive equations are considered for comparisons.

- 1) The Mendelson (1967) equation recently modified by Maneri (1995),

$$U_b = \left[ \frac{2cS}{r_l d_e} + \left( \frac{\Delta r}{r_l} \right) \frac{g d_e}{2} \right]^{1/2} \quad (1)$$

is applicable for both single gas bubbles and liquid drops rising/falling in a continuous phase of purified, low-viscosity liquids (immiscible with the drop liquid).

- 2) The Fan-Tsuchiya (1990) correlation, generalized for high-pressure systems, has a dimensionless form

$$U'_b = U_b \left( \frac{r_l}{Sg} \right)^{1/4} = \left\{ \left[ \frac{Mo^{-1/4}}{K_b} \left( \frac{\Delta r}{r_l} \right)^{5/4} d_e'^2 \right]^{-n} + \left[ \frac{2c}{d_e'} + \left( \frac{\Delta r}{r_l} \right) \frac{d_e'}{2} \right]^{-n/2} \right\}^{-1/n} \quad (2)$$

where the dimensionless bubble diameter is given by

$$d_e' = d_e (r_l g / S)^{1/2} \quad (3)$$

Three empirical parameters,  $n$ ,  $c$ , and  $K_b$ , in Eq. (2) reflect three specific factors governing the rate of bubble rise. They are the contamination level of the liquid phase, variation due to dynamic effects of the surface tension with mono- or multicomponent liquids, and the viscous nature of the surrounding medium. The suggested values of these parameters are

$$n = \begin{cases} 0.8 & \text{for contaminated liquids} \\ 1.6 & \text{for purified liquids} \end{cases} \quad (4a)$$

$$c = \begin{cases} 1.2 & \text{for monocomponent liquids} \\ 1.4 & \text{for multicomponent liquids} \end{cases} \quad (4b)$$

$$K_b = \max(K_{b0} Mo^{-0.038}, 12) \quad (4c)$$

$$\text{where } K_{b0} = \begin{cases} 14.7 & \text{for aqueous solutions} \\ 10.2 & \text{for organic solvents/mixtures} \end{cases}$$

3) The Tomiyama et al. (1995) correlation, which is given in terms of drag coefficient

$C_D = \frac{4}{3} g \Delta r d_e / (r_l U_b^2)$ , consists of three equations, depending on the system purity:

$$C_D = \max \left\{ \min \left[ \frac{16}{Re} (1 + 0.15 Re^{0.687}), \frac{48}{Re} \right], \frac{8}{3} \frac{Eo}{Eo + 4} \right\} \quad (5a)$$

for purified systems;

$$C_D = \max \left\{ \min \left[ \frac{24}{Re} (1 + 0.15 Re^{0.687}), \frac{72}{Re} \right], \frac{8}{3} \frac{Eo}{Eo + 4} \right\} \quad (5b)$$

for partially contaminated systems; and

$$C_D = \max \left[ \frac{24}{Re} (1 + 0.15 Re^{0.687}), \frac{8}{3} \frac{Eo}{Eo + 4} \right] \quad (5c)$$

for sufficiently contaminated systems.

In the above equations, i.e., Eqs. (1), (2), and (5), the dimensionless groups are defined as

$$Mo = \frac{g \Delta r m_l^4}{r_l^2 S^3}, \quad (6a)$$

$$Re = \frac{d_e U_b r_l}{\eta}, \text{ and} \quad (6b)$$

$$Eo = \frac{g \Delta r d_e^2}{S} \quad (6c)$$

where  $\Delta r = r_l - r_g$ . It is noted that  $U_b$  can be obtained explicitly from Eq. (1) or (2) for a given  $d_e$  as well as gas and liquid physical properties, while it can only be obtained implicitly from Eq. (5).

Figure 6.1 shows the predictions based on Eqs. (1), (2), and (5). For predictions, directly measured values of physical properties under various operating pressures and temperatures are used. Since the Mendelson equation, Eq. (1), is valid only under inviscid conditions, the limited agreement between the measured and calculated results at the low

temperature (Figure 6.1a) suggests that viscous forces predominate in the bubble rise process. On the other hand, at the high temperature (Figure 6.1b), there is a strong agreement over the bubble size range  $d_e > 2$  mm including the sharp breakpoint/peak. This indicates that at high temperature the liquid used in this study tends to behave as a pure inviscid liquid. Note that over the pressure range from 0.1 to 19.4 MPa, the liquid viscosity varies from 29 to 48 mPa s at 27°C, whereas it is almost constant within a range from 4.7 to 5.2 mPa s at 78°C.

The Fan-Tsuchiya (1990) correlation applied for the present liquid (Eq. (2) with  $n = 1.6$ ,  $c = 1.4$ ,  $K_{b0} = 10.2$ ) demonstrates good overall predictive capability except for the high temperature case, which exhibits a sharp peak near  $d_e = 2$  mm (see Figure 6.1b). The Tomiyama et al. (1995) equation, Eq. (5a), also has good general applicability and predicts the high temperature  $d_e = 2$  mm peak; however, it tends to underestimate the  $U_b$  values over the rest of  $d_e$  range.

The consistent difference in  $U_b$  prevailing between 0.1 and 19.4 MPa for  $d_e > 2$  mm is due to the significant increase in gas density (as large as 200-fold increase with pressure from 0.1 to 19.4 MPa). The density effect is accounted for in Eqs. (1) and (2) in terms of  $\Delta\rho/\rho_l$  or in Eq. (5) in terms of both  $\Delta\rho/\rho_l$  and  $Eu$ . As can be seen from the equations and figure, the density difference between the continuous liquid phase and the dispersed gas phase plays an important role in determining  $U_b$ , especially for large bubbles.

Figure 6.2 shows the  $Re-Eu$  relationship often utilized in representing the general rise characteristics of single bubbles in liquids (Clift et al., 1978; Bhaga and Weber, 1981). The thin background lines signify the general, quantitative trend for the rise velocity of single bubbles in purified Newtonian liquids under ambient conditions, plotted with constant intervals of  $\log Mo$ . The figure shows the general agreement in prediction between the Fan-Tsuchiya (1990) correlation (Eq. (2); solid lines) and the Tomiyama et al. (1995) equation (Eq. (5a); dot-dash lines). The present results under four conditions are plotted in the figure, along with the corresponding prediction based on Eq. (2) given by the thick solid lines. By employing accurate values for physical properties of the liquid phase and the gas density at given pressures and temperatures for Eq. (2), the experimental results can be successfully represented over the entire  $Eu$  range (i.e., bubble size range) by Eq. (2) as shown in Figure 6.2.

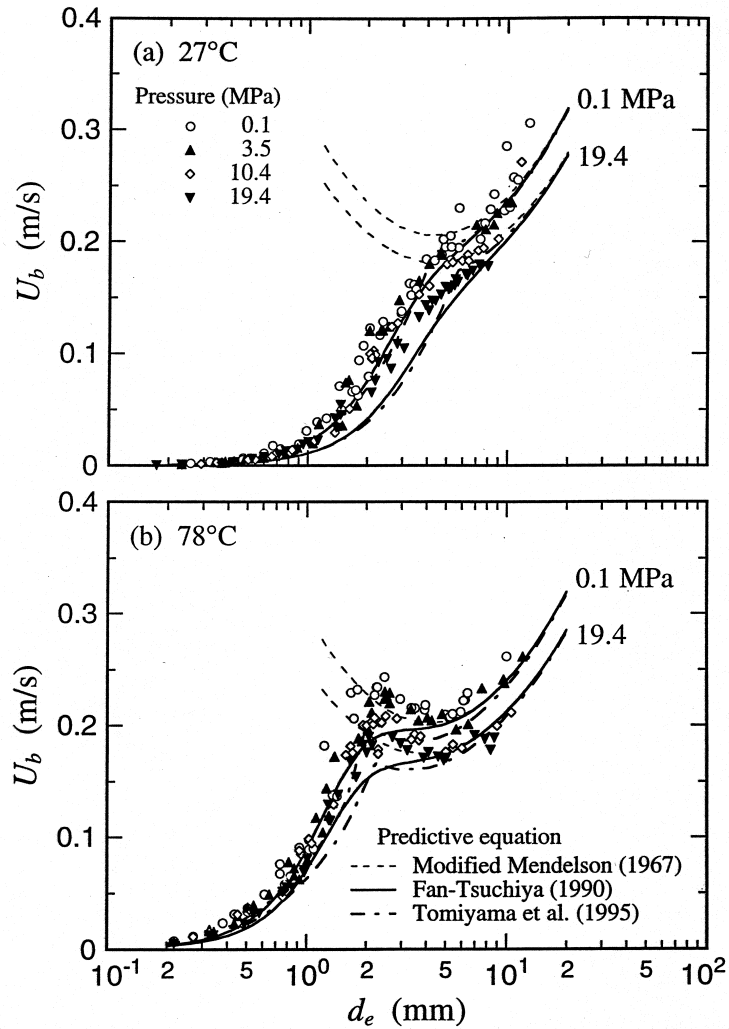


Figure 6.1. Effect of Pressure on Terminal Rise Velocity of Single Bubbles in Paratherm NF Heat Transfer Fluid and Predicted Values at (a) 27°C and (b) 78°C

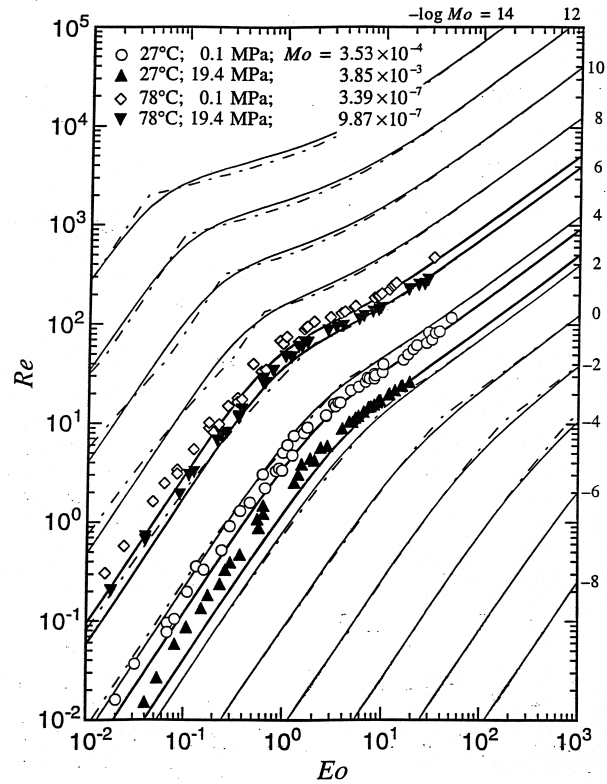


Figure 6.2. Comparisons of Measured and Calculated  $Re$  of Single Bubbles in Paratherm NF Heat Transfer Fluid Under Varied Pressure and Temperature Conditions. The Fan-Tsuchiya (1990) and Tomiyama et al. (1995) Relations are Plotted (— and — — —, respectively) at Regular Intervals of  $Mo$  Values. The Fan-Tsuchiya (1990) Correlation at Measured  $Mo$  Values for Comparison With Measured  $Re$ - $Eo$  data ( )

#### 6.4. Bubble Size Distribution

In a bubble column, bubbles undergo interactions; they can be weak as in hindered rising or strong as in coalescence and breakup. Under the hindered rising condition, the inherent rise characteristics of single bubbles play an essential role, and the initial/detached bubble size during bubble formation as well as the number density of dispersed bubbles determines the rise velocity and residence time of the bubbles in the column. For highly interactive bubbles, the dominant factor controlling their dispersion state is their dynamic size variation due to local bubble coalescence and breakup. The bubble size distribution is evaluated through direct video enhanced visualization of bubbles at a location 0.40 m above the gas distributor for various pressures under three different temperature and superficial gas velocity conditions: 27°C and 8 cm/s; 27°C and 2 cm/s; and 78°C and 5 cm/s.

As pressure increases from 0.1 to 15.2 MPa, large bubbles gradually disappear. The corresponding distributions of bubble size,  $d_b$ , from 0.6 to 4.3 mm, are shown in Figure 6.3. The shift in bubble size distribution demonstrates the effect of pressure on bubble size.

It can be seen from the figure that for pressures between 0.1 and 3.5 MPa, the bubble size is widely distributed with the fraction of bubbles of size larger than 2.5 mm decreasing noticeably with increasing pressure. For pressures greater than 7.0 MPa, the size distribution is appreciably narrower. As the pressure increases from 0.1 to 15.2 MPa, the dominant bubble size shifts from 2.5 to 0.6 mm, and the fraction of bubble sizes between 2 and 4 mm decreases by three quarters.

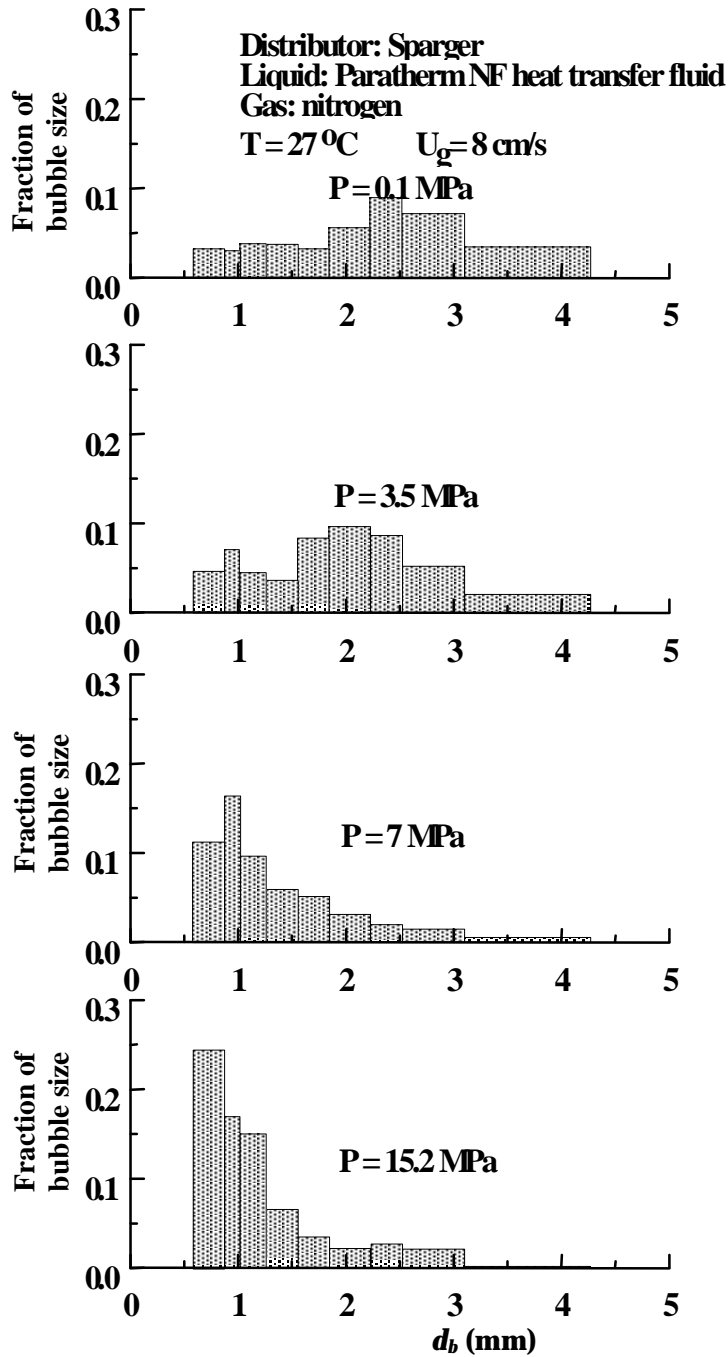


Figure 6.3. Bubble Size Distributions Under Various Pressures at  $T = 27^\circ\text{C}$  and  $U_g = 8$  cm/s

Figure 6.4 shows the associated bubble size distributions for different pressures at 27°C and  $U_g = 2$  cm/s. Again, the general trend is clearly shown that large bubbles disappear progressively with increasing pressure under both conditions. Further, the fraction of large bubbles is less at the gas superficial velocity of 2-cm/s case relative to the fraction of large bubbles at the gas superficial velocity of 8-cm/s, especially for lower pressures.

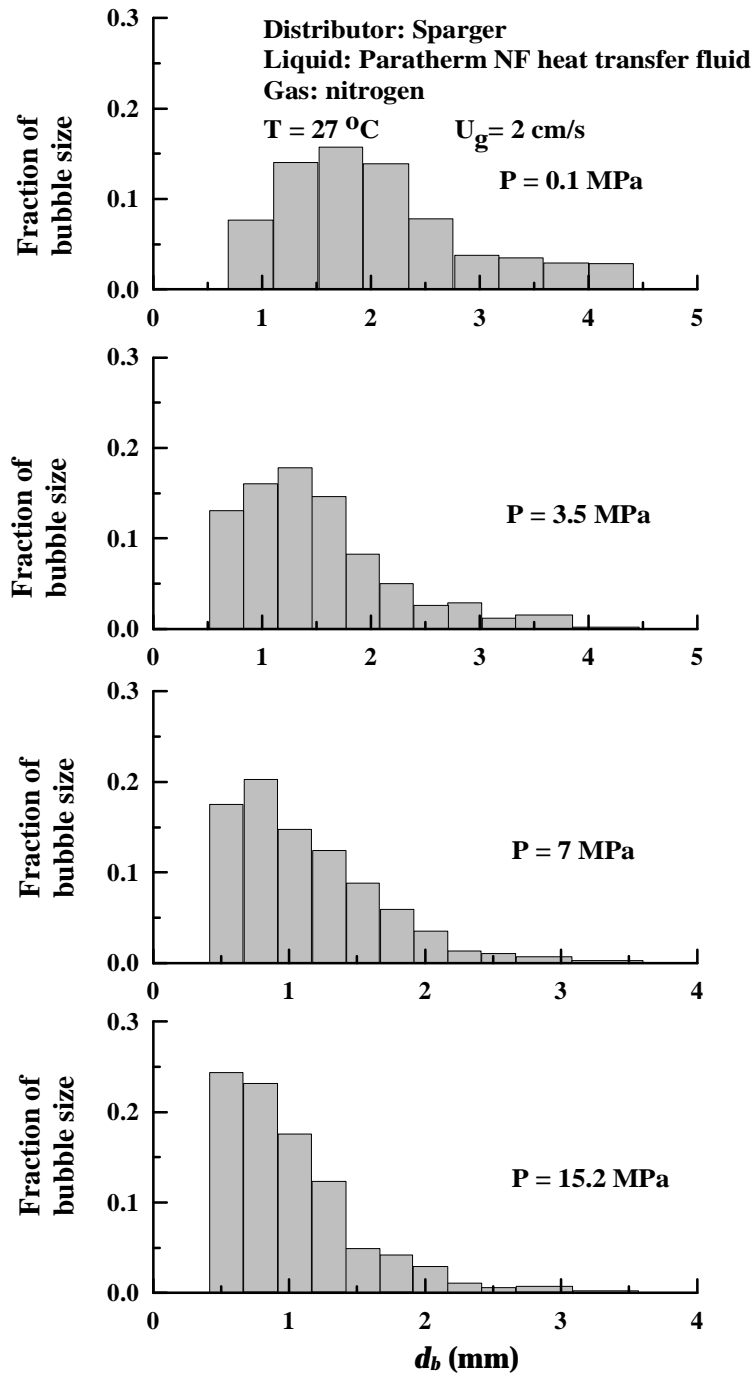


Figure 6.4. Bubble Size Distributions Under Various Pressures at  $T = 27^\circ\text{C}$  and  $U_g = 2$  cm/s

Figure 6.5 shows the corresponding bubble size distributions at 78°C and  $U_g = 5$  cm/s. As can be seen from the figure, although the most prevalent bubble size (0.5–0.6 mm) is the same for all pressures, the fraction of bubbles of size larger than 2 mm is reduced significantly as the pressure increases from 0.1 to 3.5 MPa. A comparison between Figures 6.3 and 6.5 clearly shows that, at a pressure of 3.5 MPa, the dominant bubble size is reduced from 2 mm at 27°C to 0.5 mm at 78°C.

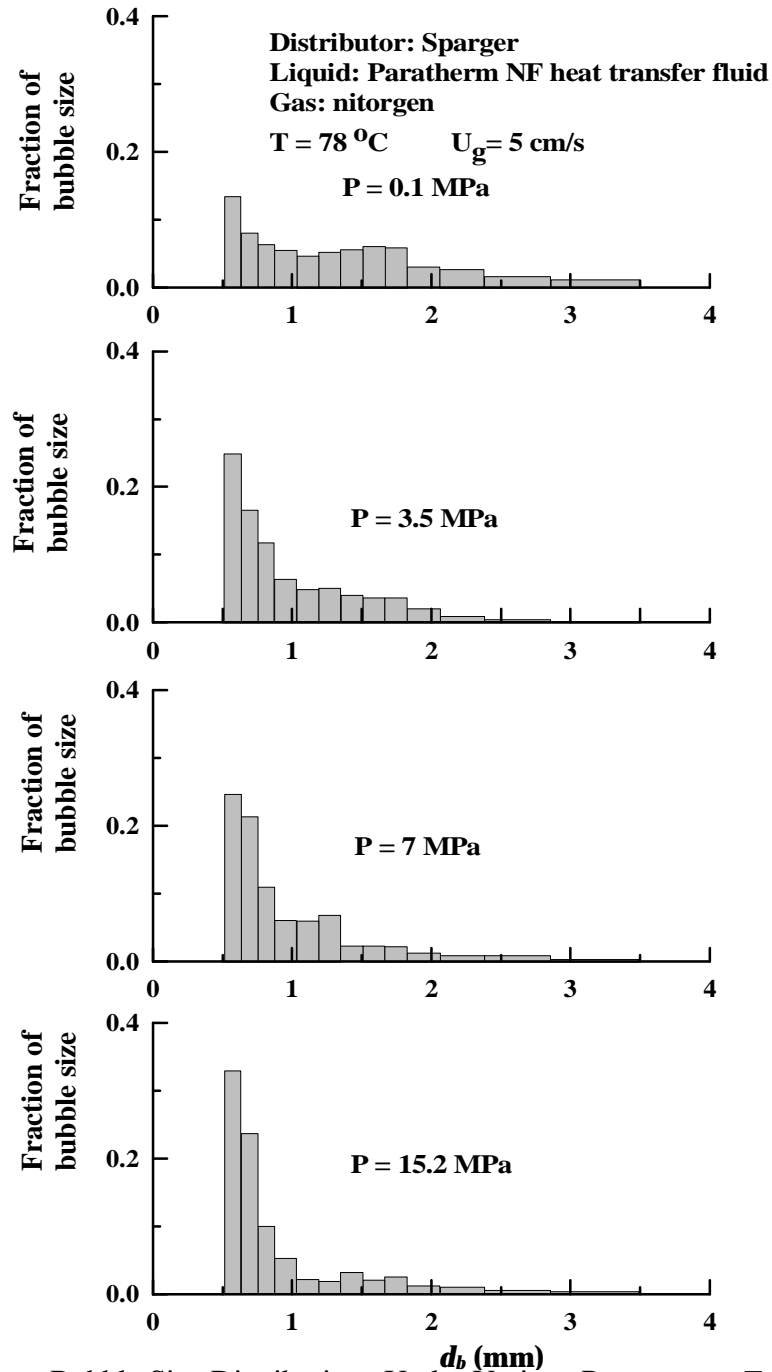


Figure 6.5. Bubble Size Distributions Under Various Pressures at  $T = 78^\circ\text{C}$  and  $U_g = 5$  cm/s

## 6.5. Theoretical Model and Numerical Method

### 6.5.1. Liquid-Phase Model

For fluidization systems, Anderson and Jackson (1967) developed the volume-averaged continuity and momentum equations. The original equations apply to both discrete and continuous phases. For the gas-liquid-solid systems, an extension of their model can lead to the volume-averaged equations for the three individual phases. In this study, the motion of particles is determined by the discrete particle method and the motion of gas bubbles is computed by a front tracking method. Thus, the averaged equations are applied only to the liquid phase.

The continuity equation can be given as

$$\frac{\partial e_l}{\partial t} + \nabla \cdot (e_l v) = 0, \quad (7)$$

and the momentum equation is

$$r_l \frac{\partial (e_l v)}{\partial t} + r_l \nabla \cdot (e_l v v) = -e_l \nabla p + e_l \nabla \cdot \tau + e_l r_l g + f_b \quad (8)$$

where  $v$  is liquid velocity vector,  $e_l$  is liquid holdup,  $r_l$  is liquid density,  $p$  is scalar pressure,  $\tau$  is viscous stress tensor,  $g$  is gravity acceleration, and  $f_b$  is total volumetric body force acting on the liquid phase other than gravity force.

The Newtonian viscous stress tensor is used which is given as

$$\tau = 2\eta S = \eta [(\nabla v) + (\nabla v)^T] \quad (9)$$

where  $S$  is the rate-of strain tensor and  $\eta$  is the kinematic viscosity coefficient.

### 6.5.2. Gas Phase Model

The gas phase is present in the form of bubbles. The flow inside the gas bubble is governed by single-phase Navier-Stokes equations. Due to the significant density difference between the gas and the liquid-solid suspension, the momentum transfer from the gas inside the bubble to the suspension is negligible except at the gas-liquid interface where the surface tension force across the interface acts on the liquid from the gas phase. Therefore, a gas bubble can be treated as a void with the motion and the topological change of its surface governed by the liquid-solid flow and the interface dynamics (Hirt and Nichols, 1981). The free surface of the gas void is reconstructed by a scalar field  $a(x,t)$ , where  $a(x,t) = 1$  in the liquid or liquid-solid mixture,  $0 < a(x,t) < 1$  at the free surface, and  $a(x,t) = 0$  in the void. The advection equation for  $a(x,t)$  is

$$\frac{\partial a}{\partial t} + (v \cdot \nabla) a = 0. \quad (10)$$

In the gas-liquid free surfaces, the stress boundary condition follows Laplace's equation as

$$p_s = p - p_v = \sigma k \quad (11)$$

where the surface pressure  $p_s$  is the surface tension-induced pressure jump across a fluid interface. The continuum surface force (CSF) model (Brackbill et al., 1992) converts the surface force into a volume force within free surfaces. The volume force at the free surfaces is given by the CSF model as

$$f_{sv}(x,t) = \sigma k(x,t) \nabla a(x,t). \quad (12)$$

This volume force is added to the volumetric body force term,  $f_b$  in the momentum equation at the free surfaces.

### 6.5.3. Dispersed Particle Model

The motion of a particle in a flow field can be described in the Lagrangian coordinates with its origin attached to the center of a moving particle. The motion of a single particle can be described by its acceleration and rotation in a non-uniform flow field. The particle accelerating in the liquid is governed by Newton's second law of motion as

$$m_p \frac{dv_p}{dt} = F_{total}. \quad (13)$$

The forces acting on a particle include interface forces between the fluid and the particle, and forces imposed by external fields. The total force acting on a particle is composed of all applicable forces, including drag, pressure gradient, added mass, gravity/buoyancy, Magnus force, Basset force, and others,

$$F_{total} = F_D + F_P + F_{AM} + F_{G/B} + \sum_i F_i. \quad (14)$$

The drag force acting on a suspended particle is proportional to the relative velocity between the phases and has the following form:

$$F_D = \frac{1}{2} C_D \rho A |v - v_p| (v - v_p) \quad (15)$$

where  $A$  is the cross-sectional area of the particle to the direction of the incoming flow,  $C_D$  is the drag coefficient, which is a function of the particle Reynolds number,  $Re_p$ . For rigid spherical particles, the drag coefficient  $C_D$  can be estimated by the following equations (Rowe and Henwood, 1961):

$$C_D = \begin{cases} \frac{24}{Re_p} (1 + 0.15 Re_p^{0.687}), & Re_p < 1000 \\ 0.44, & Re_p \geq 1000 \end{cases} \quad (16)$$

In the liquid-solid suspension, the drag force depends strongly on the local liquid holdup in the vicinity of the particle under consideration. The effective drag coefficient can be obtained by the product of the drag coefficient for an isolated particle and a correction factor as given by (Wen and Yu, 1966)

$$C_D^* = C_D e_l^{-4.7}. \quad (17)$$

The added mass force accounts for the resistance of the fluid mass that is moving at the same acceleration as the particle. For a spherical particle, the volume of the added mass is equal to one-half of the particle volume,  $V_p$ , so that

$$F_{AM} = \frac{1}{2} \rho_p V_p \frac{d}{dt} (v - v_p). \quad (18)$$

The sum of the gravity/buoyancy force and the pressure gradient force is given as

$$F_{G/B} + F_P = (\rho_p - \rho_l) V_p g - V_p \nabla p. \quad (19)$$

The general scheme of a stepwise molecular dynamic (MD) simulation (Allen and Tildesley, 1987), based on a predictor-corrector algorithm, is used to compute the particle motion. The hard sphere approach is used for the collision dynamics. The normal velocity and momentum changes of colliding particles are determined by a collinear collision model developed by Zhang et al. (1998), which includes the detailed particle-fluid and particle-particle interactions during the entire process of particle collision. In this study, the tangential velocity and momentum changes are formulated and calculated based on a sticking/sliding model.

#### 6.5.4. Coupling Among Individual Phases

When particles move into the gas-liquid interface, i.e.,  $0.5 < a(x,t) < 1$ , the surface tension force is also acting on the particle. This force equals the volumetric surface tension force  $f_{sv}$  of Eq. (12) multiplied by the particle volume. If the total force of the particle is larger than the surface tension force, the particle would penetrate the bubble surface. The penetrating particle breaks the bubble surface momentarily upon contact. If the penetrating particle is small, the bubble may recover its original shape upon particle penetration (Chen and Fan, 1989). However, if there are several particles colliding with the bubble surface simultaneously, the resulting force may cause bubble breakage.

Based on Newton's third law of motion, the total forces acting on particles yield a reaction force on the liquid. Therefore, the momentum transfer from particles to liquid is taken into account by adding the volumetric liquid-particle interaction force to the body force term,  $f_b$ , in Eq. (8).

The liquid holdup,  $e_l$ , is obtained by subtracting the volume fraction of the particles in the computational cell. A pseudo-three dimensional approach, which assumes a thickness equal to the diameter of a spherical particle for the computational cell, is used in calculating the liquid-phase holdup. The liquid properties on the particle surface are obtained by an area-weighted averaging based on the properties at the four grid points of

the computational cell containing the particle. It is found in this study that the cell averaged liquid holdup can not represent well the phase holdup surrounding a particle when the particle is within an area that has significant solids concentration variations. Therefore, the cell averaged liquid holdup is only used for solving the volume-averaged equations of the liquid phase. When using Eq. (17) to calculate the particle drag coefficient in the liquid-solid medium, the liquid holdup is obtained on the basis of a particle-centered area averaging method.

## **6.6. Results From Numerical Study**

### **6.6.1. Bubble Rising in Liquid-Solid Fluidized Medium**

A comparison of the simulation and the experimental results obtained for a single bubble rising in a liquid-solid fluidized bed is shown in Figure 6.6. The simulation domain is  $3 \times 8 \text{ cm}^2$ . One thousand particles with a density of  $2,500 \text{ kg/m}^3$  and a radius of  $0.5 \text{ mm}$  are used as the solid phase. An aqueous glycerin solution (80 wt%) with a density of  $1,206 \text{ kg/m}^3$ , a viscosity of  $5.29 \times 10^{-2} \text{ kg/m}\cdot\text{s}$  and a surface tension coefficient of  $6.29 \times 10^{-2} \text{ N/m}$  is used as the liquid phase. A spherical bubble with a diameter of  $1.0 \text{ cm}$  is initially imposed in the computational domain with its center  $1.5 \text{ cm}$  above the bottom. Initially, the particles are randomly positioned in a  $3 \times 24 \text{ cm}^2$  area. Then, the simulation is performed for the particle settling at a liquid velocity of  $0.5 \text{ cm/s}$ . At this stage, the bubble is treated as an obstacle and fixed in the original place. An equilibrium bed height is reached at  $8 \text{ cm}$ , which gives the three-dimensional equivalent solid holdups of  $0.44$ . With the particles in the equilibrium position, the simulation is restarted with bubble tracking and particle movement. The time step of simulation for liquid and solid phases is  $5 \times 10^{-6}$  second. Experiments are performed in a two-dimensional column with a thickness of  $7.0 \text{ cm}$ . The solids holdup, liquid velocity, and the liquid and solid properties are same as the simulation conditions. The time difference between two frames in Figure 6.6 is  $0.1$  second. As shown in the figure, the simulation and experimental results of the bubble rising velocity and the bubble shape generally agree well.

### **6.6.2. Particle Entrainment**

When bubbles disengage from the bed surface, particle entrainment takes place. By closely following the evolution of the particle flow around a single bubble, the mechanisms of the particle entrainment in the three-phase fluidized bed are studied experimentally by Miyahara et al. (1989), Fan and Tsuchiya (1990) and Tsuchiya et al. (1992). Their studies indicate that particles are drawn from the upper surface of the fluidized bed into the freeboard in the wake behind the bubble, and vortices containing particles are shed from the wake in the freeboard. In this study, a bubble emerging from the liquid-solid fluidized bed is simulated. The solid particles used in the simulation are glass beads with a density of  $2,500 \text{ kg/cm}^3$  and a radius of  $0.35 \text{ mm}$ . The computational domain is  $6 \times 12 \text{ cm}^2$ . Water is used as the liquid phase. The liquid velocity is set at  $7.5 \text{ cm/s}$ . The equilibrium bed height is  $6.5 \text{ cm}$  and the resulting solid holdup of the fluidized bed equals  $0.13$ . A spherical bubble with a diameter of  $0.8 \text{ cm}$  is initially imposed at  $1.5 \text{ cm}$  above the bottom. Figure 6.7 shows the bubble emerging from the bed surface in four frames of the simulation with a time difference of  $0.03$  second. Frame 1 of Figure 6.7 shows the bubble emerging from

the upper free surface of the fluidized bed. A group of particles are dragged by the bubble wake in the subsequent frames. An agreement in spatial and temporal variations of the solid particle in the entrainment process with the rising bubble is found between the simulation and the experimental results in pictures by Miyahara et al. (1989) and in sketches by Tsuchiya et al. (1992).

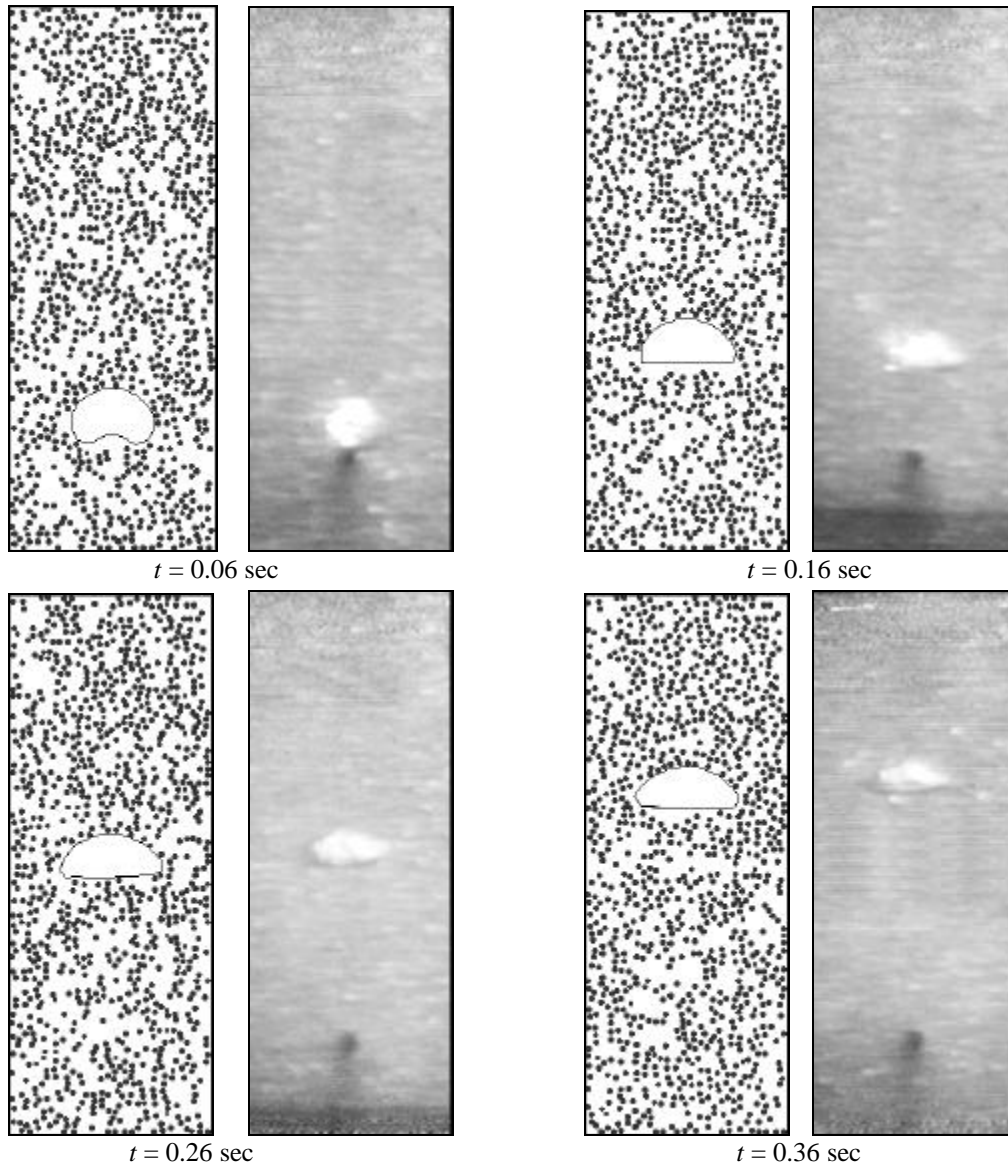


Figure 6.6. Simulation and Experimental Results of a Bubble Rising in a Liquid-Solid Fluidized Bed

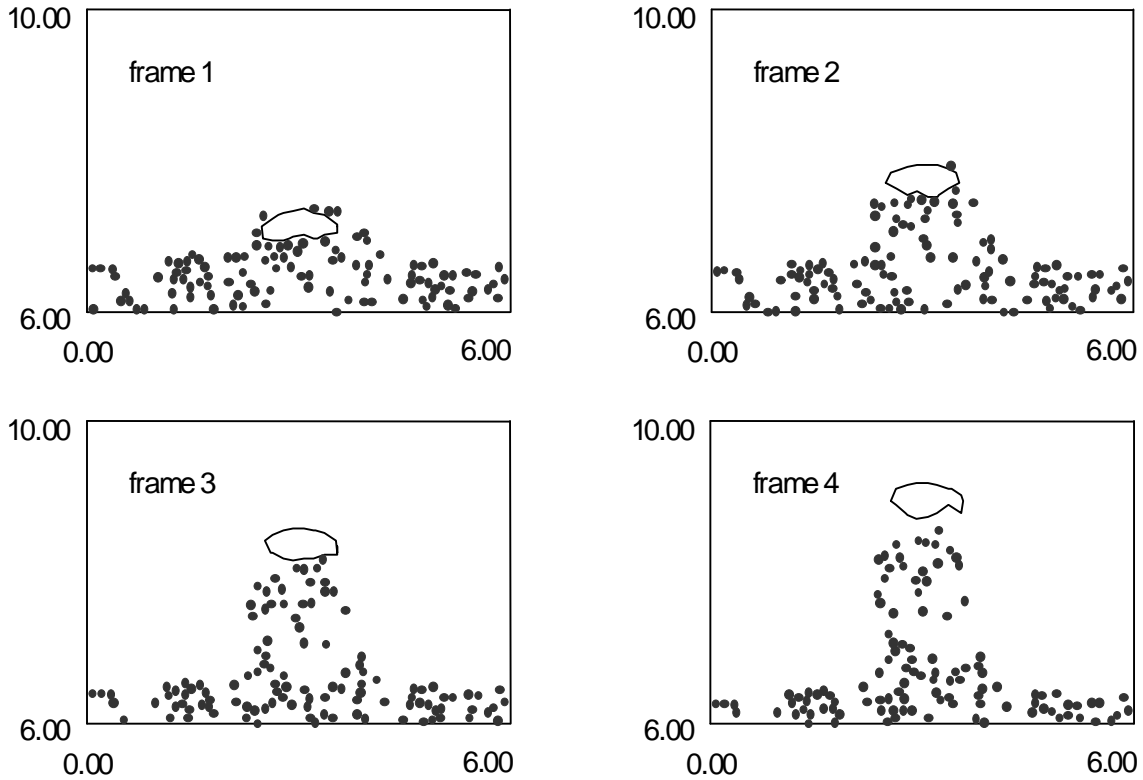


Figure 6.7. Simulation of a Bubble Emerging From a Liquid-Solid Fluidized Bed

## 6.7. References

Allen, M.P. and D.J. Tildesley, 1987. *Computer Simulation of Liquids*. Clarendon Press, Oxford.

Anderson, T.B. and R. Jackson, 1967. A fluid mechanical description of fluidized beds. *I&EC Fundam.* 6, 527-539.

Bhaga, D. and M.E. Weber, 1981. Bubbles in viscous liquids: shapes, wakes, and velocities. *J. Fluid Mech.*, 105, 61.

Brackbill, J.U., D.B. Kothe, and C. Zemach, 1992. A continuum method for modeling surface tension. *J. of Comp. Phys.* 100, 335-354.

Chen, R.C. and Fan, L.-S., 1992. Particle Image Velocimetry for characterizing the flow structure in three-dimensional gas-liquid-solid fluidized beds. *Chem. Eng. Sci.*, 47, 3615.

Chen, Y.-M. and L.-S. Fan, 1989. Bubble breakage due to particle collision in a liquid medium. *Chem. Eng. Sci.*, 44, 2762-2767.

Clift, R., J.R. Grace, and M.E. Weber, 1978. *Bubbles, Drops, and Particles*. Academic Press, New York.

Fan, L.-S., and K. Tsuchiya, 1990. *Bubble Wake Dynamics in Liquids and Liquid-Solid Suspensions*, Butterworth-Heinemann, Stoneham, MA.

Hirt, C.W. and B.D. Nichols, 1981. Volume of fluid (VOF) method for the dynamics of free boundaries. *J. Comp. Phys.*, 39, 201-225.

Maneri, C.C., 1995. New look at wave analogy for prediction of bubble terminal velocities. *AIChE J.*, 41, 481.

Mendelson, H.D., 1967. The prediction of bubble terminal velocities from wave theory. *AIChE J.*, 13, 250.

Miyahara, T.K., K. Tsuchiya, and L.-S. Fan, 1989. Mechanism of particle entrainment in a gas-liquid-solid fluidized bed. *AIChE J.*, 35, 1195-1198.

Rowe, P.N. and G.A. Henwood, 1961. Drag forces in a hydraulic model of a fluidized bed – Part I. *Trans. Instn. Chem. Engrs.*, 39, 43-54.

Tomiyama, A., I. Kataoka, and T. Sakaguchi, 1995. Drag coefficients of bubbles (First report, Drag coefficients of a single bubble in a stagnant liquid). *Nippon Kikai Gakkai Ronbunshu B Hen*, 61(587), 2357.

Tsuchiya, K., G.-H. Song, W.-T. Tang, and L.-S. Fan, 1992. Particle drift induced by a bubble in a liquid-solid fluidized bed with low-density particles. *AIChE J.*, 38, 1847-1851.

Wen, C.Y. and Y.H. Yu, 1966. A generalized method for predicting the minimum fluidization velocity. *AIChE J.*, 12, 610-612.

Zhang, J., L.-S. Fan, C. Zhu, R. Pfeffer, and D. Qi., 1998. Analytical modeling of collinear collision of elastic spheres moving at low Reynolds numbers in viscous fluids. *PTF Topical Conference at AIChE Annual Meeting*, Nov. 15-20, Miami Beach, FL.